# Structures of trehalose-6-phosphate synthase, Tps1, from the fungal pathogen *Cryptococcus neoformans*: a target for novel antifungals

Erica J. Washington[1], Ye Zhou[2], Allen L. Hsu[3], Matthew Petrovich[3], Mario J. Borgnia[3], Alberto Bartesaghi[1,2], Richard G. Brennan[1]

1. Department of Biochemistry, Duke University School of Medicine, Durham, North Carolina, 27710 USA
2. Department of Computer Science, Duke University, Durham, North Carolina, 27708 USA
3. Genome Integrity and Structural Biology Laboratory, National Institute of Environmental Health Sciences, National Institutes of Health, Department of Health and Human Services, Research Triangle Park, NC 27709 USA

[*]To whom correspondence should be addressed: richard.brennan@duke.edu

**Running Title**

Cryo-EM structures of CnTps1

**Keywords**

Tps1, Cryptococcus, cryo-electron microscopy, trehalose, fungal pathogens, Basidiomycetes

**Abstract**

Invasive fungal diseases are a major threat to human health, resulting in more than 1.5 million deaths worldwide each year. Yet the arsenal of antifungal therapeutics remains limited and is in dire need of novel drugs that target additional fungal-specific biosynthetic pathways. One such pathway involves the biosynthesis of trehalose. Trehalose is a non-reducing disaccharide composed of two molecules of glucose that is required for pathogenic fungi, including *Candida albicans* and *Cryptococcus neoformans*, to survive in their human hosts. Trehalose biosynthesis is a two-step process in fungal pathogens. Trehalose-6-phosphate synthase (Tps1) converts UDP-glucose and glucose-6-phosphate to trehalose-6-phosphate (T6P). Subsequently, trehalose-6-phosphate phosphatase (Tps2) converts T6P to trehalose. The trehalose biosynthesis pathway has been identified as a top candidate for novel antifungal development based on quality, occurrence, specificity, and assay development. However, there are currently no known antifungal agents that target this pathway. As initial steps to develop Tps1 from *Cryptococcus neoformans* (CnTps1) as a drug target, we report the structures of full-length *apo* CnTps1 and CnTps1 in complex with uridine diphosphate (UDP) and glucose-6-phosphate (G6P). Both CnTps1 structures are tetramers and display D2 (222) molecular symmetry. Comparison of these two structures reveals significant movement towards the catalytic pocket by the N-terminus upon ligand binding and identifies key residues required for substrate-binding, which are conserved amongst other Tps1 enzymes, as well as residues that stabilize the tetramer. Intriguingly, an intrinsically disordered domain (IDD), encompassing residues M209 to I300, which is conserved amongst Cryptococcal species and closely related Basidiomycetes, extends from each subunit of the tetramer into the “solvent” but is not visible in the density maps. Although, activity assays revealed that the highly conserved IDD is not required for catalysis *in vitro*, we hypothesize that the IDD is required for *C. neoformans* Tps1-dependent thermotolerance and osmotic stress survival. Characterization of the substrate specificity of CnTps1 revealed that UDP-galactose, an epimer of UDP-glucose, is a very poor substrate and inhibitor of the enzyme and highlights the exquisite substrate specificity of Tps1. *In toto*, these studies expand our knowledge of trehalose biosynthesis in *Cryptococcus* and highlight the potential of developing antifungal therapeutics that disrupt the synthesis of this disaccharide or the formation of a functional tetramer and the use of cryo-EM in the structural characterization of CnTps1-ligand/drug complexes.

54 **Introduction**

55 Invasive fungal diseases (IFDs) caused by pathogenic fungi such as *Cryptococcus*,
56 *Candida* and *Aspergillus* are a major threat to human health, resulting in more than one and a
57 half million deaths worldwide each year (1, 2). These mortality rates are surprisingly high, given
58 the fact that fungal infections are usually associated with superficial infections of skin and nails.
59 However, IFDs result in increased mortality in immunocompromised populations, including HIV-
60 infected patients and patients receiving immunosuppressive therapies (1-3). Additionally, the
61 severe acute respiratory syndrome coronavirus 2 (SARS-CoV-2; COVID-19) pandemic has
62 resulted in a significant population of COVID-19 positive patients with increased susceptibility to
63 IFDs, as has been demonstrated for pulmonary aspergillus and invasive candidiasis infections (4-
64 10).

65 Unfortunately, the current arsenal of antifungal drugs, consisting of the polyenes, azoles
66 and echinocandins, is insufficient to manage the mortality caused by IFDs due to significant off-
67 target effects, the rapid emergence of resistance to antifungal therapeutics and the emergence of
68 intrinsically drug resistant fungal pathogens, such as *Candida auris* and *Candida glabrata* (11-
69 13). Therefore, in addition to the development of new formulations of current antifungal drugs,
70 there is a critical need for the development of new classes of broad-spectrum antifungal drugs
71 that are fast-acting and safe. The identification of targets that are not present in the human host
72 is critical to the development of antifungal drugs with low toxicity. This is often difficult, as both
73 fungi and humans are eukaryotes. However, pathways involved in the fungal stress response
74 have been implicated recently as key targets, including the trehalose biosynthesis pathway (14-
75 17).

76 Trehalose is a non-reducing disaccharide composed of two glucose molecules linked by
77 an α,α-1,1-glycosidic bond. Fungal cells synthesize trehalose to protect their proteins and
78 membranes from stresses encountered during the infection process (18-25). The canonical
79 trehalose biosynthesis machinery in pathogenic fungi consists of trehalose-6-phosphate
80 synthase, Tps1, a glucosyltransferase that converts uridine diphosphate glucose (UDPG) and
81 glucose-6-phosphate (G6P) to trehalose-6-phosphate (T6P). Subsequently, trehalose-6-
82 phosphate phosphatase (Tps2), removes the phosphate group to generate the final product of
83 trehalose (Figure 1A). In *Candida albicans* and *Aspergillus fumigatus* there is an additional protein
84 in the pathway, Tps3, with no known enzymatic function. The machinery to synthesize trehalose
85 is found in plants, insects, fungi and even bacteria, but not in humans (26). For this reason, an
86 antifungal therapeutic that targets the trehalose biosynthesis pathway could well result in a drug
87 with minimal off-target effects, leading to greatly reduced toxicity in patients. Indeed, disruption of

88 the *TPS1* gene in *Cryptococcus neoformans* results in fungi that are avirulent in mice and rabbits
89 and, interestingly, disruption of *TPS2* was followed by the accumulation of the toxic intermediate
90 trehalose 6-phosphate, causing fungal cell death (27). Additionally, in *C. neoformans* trehalose
91 acts as a stress protectant and is required for growth at high temperatures (27). Similarly,
92 disruption of the *TPS1* and *TPS2* genes in *Cryptococcus gattii* results in decreased infectivity in
93 mice (28). Similar phenotypes indicating the importance of Tps1 and Tps2 to cell survival and
94 sometimes virulence are also seen in trehalose biosynthesis mutants in *C. albicans* (29-31) and
95 *A. fumigatus* (32, 33). Therefore, we hypothesize that targeting the trehalose biosynthesis
96 pathway will result in the development of a novel broader-spectrum antifungal drug, which would
97 be both highly effective and, importantly, safe for use in immunocompromised patients.
98 Pertinent to the development of an antifungal therapeutic which targets the trehalose
99 biosynthesis pathway is an intimate knowledge and understanding of the structures of enzymes
100 and proteins involved in this important pathway. Several structures of Tps1 and Tps2 from
101 nematodes, bacteria and pathogenic fungi have been determined using x-ray crystallography (34-
102 43). Subsequently, compounds that inhibit trehalose biosynthesis enzyme functions by targeting
103 their catalytic pockets have been investigated but not yet advanced for clinical use (39, 44-49).
104 As a key starting point to develop inhibitors of CnTps1, we describe structures of this 669-residue
105 (74 kDa per protomer) enzyme in both its *apo* (substrate-free) form and in complex with UDP and
106 G6P using single particle cryo-electron microscopy (cryo-EM). Unlike Tps1 from *Candida albicans*
107 (40), CnTps1 has three major insertions, 55 residues at the N-terminus, 63 residues at the C-
108 terminus and a 92-residue intrinsically disordered domain (IDD) inserted within the core of the
109 enzyme, all of unknown function. Residues located in the catalytic pocket and the IDD were
110 assayed for their contribution to the activity of this enzyme. Intriguingly, the IDD of CnTps1 is not
111 required for CnTps1 catalytic activity *in vitro*. Substrate specificity was investigated further and
112 revealed the exquisite ability of CnTps1 to discriminate at the level of a single interaction. Hence,
113 this work lays the groundwork for subsequent CnTps1 structure-based drug design.

114 **Results**

115 **Trehalose biosynthesis protein CnTps1 self-associates in bacterial two-hybrid assays**

116 The trehalose biosynthesis pathway is a two-step process. Tps1, trehalose-6-phosphate
117 synthase, converts uridine diphosphate glucose (UDPG) and glucose-6-phosphate (G6P) into
118 trehalose-6-phosphate (T6P). The phosphate group is subsequently removed from T6P by
119 trehalose-6-phosphate phosphatase (Tps2) to yield trehalose (Figure 1A) (17). Previously the
120 structures of Tps1/OtsA from *Candida albicans* (40), *Aspergillus fumigatus* (40), *E. coli (35, 37,*
121 *38, 43)*, *Streptomyces venezuelae* (34) and *Magnaporthe oryzae* (43) were determined using x-
122 ray crystallography. Additionally, the structure of the catalytically inactive Tps1-like N-terminal
123 domain of *C. albicans* Tps2 was determined (41).

124 Inspection of the Tps1 crystal structures from *Candida albicans* (40), *Aspergillus fumigatus*
125 (40), *E. coli* (37, 38), *Streptomyces venezuelae* (34) and *Magnaporthe oryzae* (43) and the
126 catalytically inactive Tps1-like N-terminal domain of *C. albicans* Tps2 (41) revealed that Tps1
127 most likely exists as a homo-tetramer. To determine if subunits of the *Cryptococcus neoformans*
128 var. *grubii* strain H99 Tps1, hereafter referred to as CnTps1, self-associate, a bacterial two-hybrid
129 system based on the LexA DNA-binding repressor was established (50). Expression of full-length
130 LexA-CnTps1 in the bacterial two-hybrid system was not detected. However, LexA-CnTps1$_{56\text{-}669}$,
131 in which the unstructured 55 N-terminal residues of CnTps1 were deleted, does self-associate in
132 the bacterial two-hybrid assay, as evidenced by a reduction in β-galactosidase activity after
133 protein expression was induced with 1 mM IPTG (Figure 1B). An anti-LexA Western blot shows
134 the expression of LexA-CnTps1$_{56\text{-}669}$ at the appropriate molecular weight (Figure 1C). These data
135 indicate that CnTps1 can self-associate and support the hypothesis that CnTps1 forms homo-
136 oligomers.

137

138 **The structure of the *apo* (substrate-free) CnTps1 homo-tetramer**

139 CnTps1 is approximately 200 residues larger than other Tps1 orthologues, due to the
140 addition of a 55-residue N-terminal extension, a 63-residue C-terminal extension and an internal
141 insertion from residues M209 to I300 (Supplemental Figure 1). Each extension is predicted to be
142 structurally disordered. In order to determine the structure of CnTps1, the full-length (74 kDa, 669-
143 residue per protomer) CnTps1 protein was expressed with an N-terminal hexahistidine tag and
144 purified from *E. coli* via $Ni^{2+}$-NTA affinity chromatography (Supplemental Figure 2A). Following
145 confirmation that 6xHis-CnTps1 was enzymatically active (Supplemental Figure 2B), the protein
146 sample was subjected to single particle cryo-electron microscopy analysis. 2,520 micrographs
147 were collected from grids prepared with 6xHis-CnTps1 (Supplemental Figure 3). No additional

148 ligands were added to the protein sample. 2D classification, performed on 907 micrographs with
149 resolution higher than 4.0 Å, revealed tetrameric CnTps1 particles (Supplemental Figure 3). 3D
150 classification and initial refinement steps were performed without imposing symmetry
151 (Supplemental Figure 3), resulting in a 5.3 Å resolution map. Additional refinement and polishing
152 steps, including adding D2 symmetry, resulted in an *apo* CnTps1 map at 3.3 Å global resolution,
153 as estimated by the "gold standard" Fourier shell correlation (FSC) = 0.143 criteria (Data Table 1
154 and Supplemental Figure 4A,B). Four protomers can be readily differentiated in the *apo* CnTps1
155 cryo-EM map (Supplemental Figure 4C). The final map shows features of well-resolved side
156 chains of many amino acid residues (Supplemental Figure 4D). The atomic model for *apo*
157 CnTps1, which was built based on the cryo-EM reconstruction, supports the conclusion that *apo*
158 CnTps1 forms a homo-tetramer (Figure 2).
159 The four CnTps1 protomers of the tetramer, designated as protomers 1 – 4, assemble into
160 the tetrameric structure with dimensions of 100.0 x 110.3 x 107.6 Å (Figure 2A-C). The four
161 protomers interact via two α-helical domains that are found in the central region of the homo-
162 tetramer (Figure 2A). The unbound substrate-binding pockets, are open and outward-facing, and
163 therefore accessible to ligands and substrates (Figure 2A,B). The "bottom-facing" view of the
164 homo-tetramer shows a staggered appearance of the top and bottom pair of protomers (Figure
165 2C).
166 Each CnTps1 protomer is comprised of N and C-terminal lobes, containing residues 1-
167 378 and 379-669, respectively. Both lobes are spanned by an α-helix, formed by residues 572-
168 603 (Figure 2D). Each domain contains a modified Rossman fold that is characteristic of the
169 retaining glycosyltransferase family (40, 51) (Figure 2D), and similar to the published CaTps1 and
170 CaTps1-like N-terminal domain of CaTps2 structures (Supplemental Figure 5) (34, 41, 43). A
171 common feature that is observed in these substrate-free structures is a lack of density in portions
172 of the N-terminus, suggestive of conformational flexibility in the absence of ligands. Indeed, the
173 CnTps1 cryo-EM map shows clear density for secondary structures in the C-terminus, whilst the
174 density was poor in several parts of the N-terminal domain, including that for residues 1-58, 68-
175 100, 127, 180, 210-301, 354-357 and 364-368 (Figure 2D). Not unexpectedly, the N-terminus
176 extension, the C-terminus and the internal insertion, residues 209-300, are not visible in this
177 structure suggesting multiple accessible conformations or intrinsic disorder.
178
179 **The structure of the CnTps1-UDP-G6P complex**
180 In order to identify residues in the catalytic pocket of CnTps1 as well as to visualize any
181 conformational changes necessary for substrate binding and catalysis, we determined the cryo-

182 EM structure of the *C. neoformans* H99 Tps1 in complex with the substrate, G6P, and a product,
183 UDP, to 3.1 Å global resolution (Figure 3A-D). 3,182 movies were collected from grids prepared
184 with 6xHis-CnTps1 and an excess of UDP and G6P (Supplemental Figure 6). The 2D
185 classification revealed tetrameric structures like those observed for *apo* CnTps1 (Supplemental
186 Figure 6). The cryo-EM reconstruction of 6xHis-CnTps1 bound to UDP and G6P also revealed a
187 tetrameric assembly. Final refinement was performed with D2 symmetry imposed (Supplemental
188 Figure 6). The addition of G6P and UDP resulted in a higher global resolution of the CnTps1
189 structure when compared to the *apo* structure (Data Table 2). The substrate-binding pocket is
190 more ordered (Supplemental Figure 7A,B). Four protomers can be detected in the CnTps1-UDP-
191 G6P cryo-EM map (Supplemental Figure 7C) and the final map shows features of well-resolved
192 side chains (Supplemental Figure 7D).
193 As observed in the *apo* structure, the N and C-termini and the internal insertion remain
194 unstructured in the presence of ligands. The structure of CnTps1 bound to UDP and G6P is similar
195 to that of the published CaTps1-UDP-G6P complex and the N-terminus of CnTps2 with root mean
196 square deviations (rmsds) of 1.2 Å for 450 corresponding $C_\alpha$ atoms and 1.5 Å for 468
197 corresponding $C_\alpha$ atoms, respectively (40, 41, 52). Views of the CnTps1-UDP-G6P tetramer show
198 the central binding region of UDP and G6P inside each protomer (Figure 3A-D). A view of each
199 protomer of the CnTps1-UDP-G6P complex reveals the substrate-binding site, with the UDP
200 bound to the C-terminal domain and the G6P adjacent to the N-terminal domain (Figure 3D). The
201 binding sites of the ligands are in excellent agreement with the published structure of CaTps1-
202 UDP-G6P and CaTps1-UDPG (40).
203
204 **Ligand-induced conformational changes in *C. neoformans* Tps1**
205 Significant movement and conformational changes of the N-terminal domain are observed
206 due to ligand binding to CnTps1 (Figure 4A,B). Structural alignments of the individual N-terminal
207 domain (residues 56 – 378) and C-terminal domain (residues 379 – 603) of the *apo* Tps1 protein
208 onto the corresponding domains of UDP-G6P bound CnTps1 reveal rmsds of 1.1 and 0.4 Å,
209 respectively. Superposition of the complete structure of *apo* CnTps1 onto CnTps1-UDP-G6P
210 reveals an rmsd of 1.4 Å for 433 corresponding $C_\alpha$ atoms. These rmsd values are a result of
211 ligand-induced conformational "closing" and stabilization of CnTps1, with the movement occurring
212 primarily in the N-terminus. Thus, *apo* CnTps1 protomers are in a more "open" conformation as
213 compared to the ligand-bound subunits. Systematic analysis of the domain movements using the
214 program DynDom (53, 54) shows that the large movements of the N-terminal G6P-binding lobe
215 centered around α-helix 2 (residues 112 to 125), which is located on the surface of the N-terminal

216 domain, result in a rotation of approximately 20° (Supplemental Figure 8). This rotation causes
217 an inward, approximately 7 Å, movement of α-helix 2 (Figure 4B). The linker that facilitates this
218 movement includes residues 113 through 145. This rotation results in a 29% closure of the N and
219 C-terminal lobes around the substrate-binding pocket. Interestingly, the local resolution proximal
220 to CnTps1 α-helix 2 is the lowest in the structure, which may indicate flexibility and a propensity
221 for movement, consistent with the results of the DynDom analysis. Since the CnTps1-UDP-G6P
222 complex contains both a product (UDP) and a substrate (G6P) as ligands, the completely closed
223 form of the protein is likely not visualized in this structure. Regardless, the movement of this
224 domain would facilitate the $S_N$-i catalytic mechanism proposed for Tps1 proteins in the GT-B fold
225 retaining glycosyltransferase family, including *C. albicans* Tps1 and *E. coli* OtsA (35, 40, 51, 55).
226 Indeed, superposition of UDP onto the UDPG from the CaTps1-UDPG complex (PDB ID 5HUT)
227 reveals that the G6P substrate bound to CnTps1 is proximal to and properly aligned with the
228 glucose of the UDPG to allow the ready formation of the 1,1 glycosidic bond, required for the
229 formation of T6P (Supplemental Figure 9).
230
231 **CnTps1 substrate-binding residues**
232 We were able to detect strong density for the bound ligand and substrate-binding residues
233 of CnTps1 (Figure 5A). The UDP molecule is bound to the C-terminal portion of each protomer
234 (Figure 5B). The orientation of the uracil base and CnTps1 is mediated by a hydrogen bond
235 between the exocyclic O4 and the V492 amide NH group. The O2 and O3 hydroxyl groups of the
236 ribose ring of UDP form hydrogen bonds with the side chain of E522. The orientation of the
237 phosphate groups of UDP in CnTps1 is mediated by several interactions. One hydrogen bond is
238 made between the α-phosphate group and the backbone amide group of L518. In CaTps1 (40)
239 there is a conserved Arg-Lys pair (residues R280 and K285) that interacts with the phosphate.
240 We were unable to detect side chain density for the equivalent CnTps1 Arg, indicating movement
241 of the substrate-binding pocket, potentially ready to release the product UDP. There is, however,
242 a hydrogen bond between K420 and the β-phosphate. Based on an overlay with the CaTps1-
243 UDPG structure, we predicted that the glucose moiety in the native substrate, UDPG, would be
244 stabilized by CnTps1 D514 and positioned to deprotonate G6P (Figure 5B and Supplemental
245 Figure 10A) (40). The G6P molecule is located adjacent to the N-terminal lobe in each protomer.
246 A key interaction stabilizing G6P is residue R453, which forms hydrogen bonds and ionic
247 interactions with the G6P phosphate group (Figure 5C).
248 CnTps1 substrate-binding residues K420, D514, L518, E522 and R453 are conserved
249 amongst Tps1 proteins from *C. neoformans*, *C. albicans*, *A. fumigatus*, *M. oryzae*, *S. venezuelae*

250 and *E. coli* (Supplemental Figure 1 and Supplemental Figure 10B). In *C. albicans* Tps1 these
251 residues have been demonstrated to be required for hyphal development and thermotolerance
252 (40). Site-directed mutagenesis was used to generate variants of CnTps1 in which potential
253 substrate-binding residues were mutated as follows: E522A, K420A, D514A and R453A. All
254 CnTps1 variants eluted similarly to wild-type CnTps1 on the size exclusion column, indicating that
255 they are properly folded (Supplemental Figure 11). Tps1 coupled enzyme assays revealed that
256 mutation of the residues that interact with UDP/UDPG resulted in severe loss-of-function (Figure
257 5D). Mutation of R453 to an alanine, which is the single identified G6P-interacting residue,
258 resulted in greatly reduced CnTps1 activity as well (Figure 5E).
259
260 **Interactions within the CnTps1 homo-tetramer**
261 The interactions between several side chains in the interfaces between CnTps1 protomers
262 explain the formation and stabilization of the CnTps1 homo-tetramer. The two key interfaces
263 responsible for formation of the CnTps1 homo-tetramer are referred to as interface #1 and
264 interface #2 (Supplemental Figure 12A). According to PDBePISA analysis (56), the buried surface
265 areas for each interface are similar, with 1062.9 Å buried in interface #1 and 986.2 Å buried in
266 interface #2. Interestingly, the calculated free energy (ΔG) of the two interfaces is -10.7 kcal/mol
267 and 0.1 kcal/mol, respectively, which suggests the former interface is a critical component of
268 oligomerization.
269 The key interactions in interface #1 are the hydrogen bonds between N467 and E468, as
270 well as R403 and E481 (Supplemental Figure 12B,C). Interface #2 also has hydrogen bonds that
271 are critical to the stability of the homo-tetramer, including hydrogen bonds between the E314
272 backbone oxygen and R513 side chain (Supplemental Figure 12D). Ionic interactions between
273 R513 and E314 and between R322 and E538 also contribute to the formation of interface #2.
274 None of the interface residues directly contact UDP or G6P, indicating that any effect mutation of
275 these residues might have on activity would be allosteric. Our cryo-EM results confirm that the
276 homo-tetrameric form of CnTps1 accurately represents the tetrameric structure in solution and is
277 not an artifact of the crystal lattice packing.
278
279 **CnTps1 contains a conserved intrinsically disordered domain**
280 As described above, CnTps1 contains three unstructured insertions (Supplemental Figure
281 13A). These regions have likely prevented the determination of its structure with x-ray
282 crystallography, as these regions are the main differences between CnTps1 and other crystallized
283 Tps1 orthologues, such as CaTps1. The most prominent unstructured region in CnTps1 is an

284 internal insertion of 92 residues (residues M209-I300), referred to hereafter as the Intrinsically
285 Disordered Domain or IDD (Supplemental Figure 13A). Interestingly, the CnTps1 IDD is found
286 only in the Tps1 proteins in fungi within the fungal division, Basidiomycota (Supplemental Figure
287 13B). More specifically, the CnTps1 IDD is highly conserved within Cryptococcal species and
288 closely related Basidiomycetes, with *C. neoformans*, *C. gattii* and *C. deneoformans* containing
289 IDDs with greater than 92% identity (Supplemental Figure 13A,B). The CnTps1 IDD is not present
290 in the Ascomycota division or the Mucoromycota phylum (Supplemental Figure 13B).
291 As anticipated, density for the CnTps1 IDD was not detected in the structures of *apo*
292 CnTps1 or CnTps1-UDP-G6P, consistent with the idea that the IDD is conformationally flexible.
293 However, based on the CnTps1 structures, we can determine that the IDD exits and returns to
294 the structured regions in adjacent parts of the N-terminus of CnTps1. To determine if the IDD is
295 required for CnTps1 activity *in vitro*, we designed and purified a chimeric protein in which the 92-
296 residue CnTps1 IDD was replaced with the six residues (GNKKKN), which *C. albicans* Tps1
297 utilizes to connect α-helix 5 to β-strand 4 (Supplemental Figure 14). We refer to this protein as
298 CnTps1 ΔIDD.
299 To determine the effect that the CnTps1 IDD has on CnTps1 function, we purified CnTps1
300 ΔIDD and confirmed that it was reduced in size compared to wild-type CnTps1, as determined by
301 size exclusion chromatography (Supplemental Figure 11). Notably, deletion of the CnTps1 IDD
302 did not affect formation of the tetramer (Supplemental Figure 11). Circular dichroism experiments
303 also confirmed that CnTps1 ΔIDD is properly folded (Supplemental Figure 15). Coupled enzyme
304 activity assays with CnTps1 ΔIDD were performed and revealed that the CnTps1 IDD is not
305 required for enzymatic activity of CnTps1 *in vitro* (Supplemental Figure 13C).
306
307 **Specificity of CnTps1 catalytic pocket**
308 To assess the substrate specificity of the CnTps1 catalytic pocket, we tested the catalytic
309 activity of CnTps1 in the presence of UDP-Galactose (UDP-Gal). The hydroxyl group on the 4$^{th}$
310 carbon is oriented in opposite orientation in glucose and galactose. In the CaTps1-UDPG
311 structure, all of the extracyclic hydroxyl groups are easily detected, revealing that the O4 hydroxyl
312 hydrogen forms a hydrogen bond with the peptide backbone of CaTps1 N382 (40). Similarly, the
313 peptide backbone of CnTps1-UDP-G6P N517 would interact with the O4 hydroxyl of the glucose
314 moiety of UDPG (Supplemental Figure 16A). Modeling UDP-Galactose into the catalytic pocket
315 reveals the O4 hydroxyl points away from N517, preventing the formation of this critical hydrogen
316 bond (Supplemental Figure 16B). The loss of this interaction has a drastic effect on the activity of
317 CnTps1 with UDP-Gal as demonstrated by a reduction of approximately 96%, compared to

318 CnTps1 with UDPG as a substrate (Figure 6A), suggesting that the correct positioning of the O4
319 hydrogen mediated by its interaction with N517 is required for CnTps1 activity. This interaction
320 likely helps orient the entire UDPG molecule in the CnTps1 substrate-binding pocket for efficient
321 substrate-assisted catalysis.

322 To further explain the effect of UDP-Gal on CnTps1 activity, we performed a competition
323 assay. The combination of equal molar ratios of UDPG and UDP-Gal to CnTps1 resulted in a 12%
324 reduction in activity, compared to only adding UDPG to the assay (Figure 6B). Interestingly, the
325 addition of 10-fold excess UDP-Gal compared to UDPG resulted in a reduction of CnTps1 activity
326 by approximately 30% (Figure 6B), indicating that UDP-Gal is capable of binding CnTps1 but is a
327 weak binder and likely a weak competitive inhibitor, by binding to the substrate-binding pocket of
328 CnTps1.

329 **Discussion**

330 In order to develop the trehalose biosynthesis pathway as an antifungal drug target, we
331 must improve our understanding of the structure and function of trehalose biosynthesis proteins.
332 Here we report the use of cryo-EM to determine the structures of *apo* CnTps1 and CnTps1 bound
333 to UDP and G6P.

334 We confirmed that CnTps1 forms a tetramer in solution, indicating that previously reported
335 structures of Tps1 proteins determined by x-ray crystallography and exhibiting tetrameric
336 complexes are not simply an artifact of the crystal lattice packing. Our current hypothesis is that
337 trehalose biosynthesis proteins also form hetero-tetrameric complexes. Interactions amongst Tps
338 proteins (Tps1, Tps2, Tps3 and Tsl1) have been demonstrated in *S. cerevisiae* (57, 58). The
339 function of these complexes may be to sequester the highly cytotoxic trehalose-6-phosphate
340 (T6P) from the cytoplasm, to target trehalose biosynthesis to a proper subcellular localization (59)
341 or to allow for quick and efficient production of trehalose when fungal pathogens are exposed to
342 environmental stress. Future work shall include confirmation of the formation of heterocomplexes
343 both *in vitro* and *in vivo* and determination of the structure of the heterocomplex using cryo-
344 electron microscopy.

345 We have also reported here a conformational change of the individual protomers of
346 CnTps1 upon binding of UDP and G6P. Comparison of the *apo* CnTps1 and CnTps1-UDP-G6P
347 structures reveals an inward movement of the N-terminus of CnTps1 when bound to ligand. Most
348 of the movement occurs in α-helix 2 and surrounding residues. The closure of the ligand-bound
349 CnTps1 protomer is consistent with substrate-assisted catalysis, the proposed enzymatic
350 mechanism of Tps1 enzymes. Consistent with previous reports of the predicted catalytic activity
351 of fungal Tps1 proteins, we also propose that UDPG binds first, followed by G6P. The proximity
352 of the substrates in the substrate-binding pocket of CnTps1 is demonstrated in Supplemental
353 Figure 9. However, we now can see aspects of the catalytic mechanism occurring in the context
354 of the CnTps1 homo-tetramer for the first time.

355 The more ordered CnTps1-UDP-G6P substrate-binding pocket allows us to observe
356 specific interactions between the ligands and CnTps1 substrate-binding residues. The
357 identification of substrate-binding residues, K420, D514, E522 and R453, provides key insights
358 into the mechanism of the Tps1 glycosyltransferase as well as demonstrates the key roles of
359 these residues in substrate specificity (Figure 5A-C). Mutation of any of these residues is sufficient
360 to inhibit CnTps1 catalytic activity (Figure 5D,E). Additionally, our determination of substrate-
361 binding variants which lead to a loss of activity of CnTps1 provides the framework for further
362 investigation of a fully closed substrate-trapped cryo-EM structure of the CnTps1 homo-tetramer

363 in the future. This structure will provide fuller information regarding the CnTps1 catalytic
364 mechanism by allowing visualization of CnTps1 bound to the native substrates, UDPG and G6P.
365 The substrate-binding residues identified in the catalytic pocket of Tps1 are highly
366 conserved amongst fungal pathogens, including *C. albicans* (Supplemental Figure 1 and
367 Supplemental Figure 10B), supporting the proposition that a broader-spectrum antifungal
368 therapeutic can be developed by targeting the catalytic pocket of Tps1. Additionally, we have
369 been able to demonstrate that the CnTps1 substrate-binding domain is highly specific and
370 constrained as underscored by its inability to utilize UDP-Galactose as a substrate, which is an
371 epimer of UDPG (Figure 6 and Supplemental Figure 16).
372 Although the key interfaces of the CnTps1 homo-tetramer are not as highly resolved as
373 the substrate-binding pocket, specific residues that may play a role in the formation of the homo-
374 tetramers were identified (Supplemental Figure 12). It remains to be determined whether
375 tetramerization of CnTps1 is required for catalytic activity. We have evidence that disruption of *C.*
376 *albicans* Tps1 oligomers, achieved by the mutation of two residues, results in a significant
377 reduction of the ability of CaTps1 to generate T6P and also prevents strains of *C. albicans tps1*Δ
378 expressing monomeric Tps1 from proliferating in mice (data not published). Therefore, in addition
379 to targeting the substrate-binding pocket of CnTps1, the interfaces critical to the formation of the
380 CnTps1 tetramer may also be novel antifungal drug targets.
381 Finally, we have studied the importance of a 92-residue (residues M209-I300)
382 unstructured region in CnTps1, now called the intrinsically disordered domain (IDD)
383 (Supplemental Figures 1 and 13A). Interestingly, the IDD is well-conserved amongst Cryptococcal
384 species and closely related fungi in the Basidiomycota division (Supplemental Figure 13B). We
385 have also demonstrated, with the generation of a CnTps1 ΔIDD protein, that these 92 residues
386 are not required for the catalytic activity of CnTps1 *in vitro* (Supplemental Figure 13C). These
387 data are consistent with the residues neither interacting with CnTps1, either intra- or inter-
388 molecularly, nor being proximal to the catalytic region of CnTps1.
389 CnTps1 is required for the growth of *C. neoformans* at high growth temperatures, 37 °C
390 (27). In the future, we shall determine if the CnTps1 IDD is critical for the survival of *C. neoformans*
391 at high temperatures and in the presence of osmotic stress, both of which are encountered when
392 *C. neoformans* transitions from the environment to the human host. We posit, therefore, that the
393 main function of the CnTps1 IDD may involve its posttranslational modification, protein-protein
394 interactions and/or targeting CnTps1 to specific subcellular localizations in fungal cells. Future
395 work to determine the function of the CnTps1 IDD will aid in the development of the CnTps1 IDD
396 as a novel Basidiomycete-specific antifungal drug target.

397 In summary, we have solved the first cryo-EM structure of a Tps1 homo-tetramer, the
398 formation of which is potentially required for efficient trehalose biosynthesis and is therefore a
399 viable antifungal drug target (Supplemental Figure 17). We identified key residues that play a role
400 in tetramerization, as well as conserved substrate-binding residues. We have demonstrated that
401 the substrate-binding site of Tps1 is highly conserved and specific for UDPG. Finally, we identified
402 a novel 92-residue insertion in CnTps1 that may contribute to *C. neoformans* Tps1-mediated
403 tolerance of temperature and osmotic stress, both of which are encountered in the human host.
404 In conclusion, our work presented here will facilitate the development of novel antifungal drugs
405 which target multiple aspects of the trehalose biosynthesis pathway.

406 **Materials and Methods**

407

408 **Bacterial two-hybrid**

409 Protein interactions were analyzed by a bacterial two-hybrid analysis based on a set of
410 vectors described by Daines and Silver (60). The genes for *C. neoformans Tps1* were cloned into
411 the plasmid pSR658, which contains an N-terminal LexA DNA-binding domain. The resulting
412 plasmid was cloned into *E. coli* strain SU101 to test for homo-oligomerization and expression of
413 the protein fusions was induced with 1 mM IPTG. For this purpose, 5 mL of LB culture
414 supplemented with antibiotics were inoculated and grown to 0.5 to 0.6 OD600 at 37 °C. The
415 culture was mixed with permeabilization buffer (100 mM $Na_2HPO_4$, 20 mM KCl, 2 mM $MgSO_4$, 0.8
416 mg/mL CTAB, 0.4 mg/mL deoxycholic acid sodium salt, and 5.4 µL/mL of β-mercaptoethanol).
417 Samples were incubated at 30 °C for 30 minutes and subsequently incubated with the prewarmed
418 substrate solution (60 mM $Na_2HPO_4$, 40 mM $NaH_2PO_4$, 1 mg/mL ONPG, 2 µL/mL of β-
419 mercaptoethanol). After 25 minutes, the stop solution (1 M $Na_2CO_3$) was added, and the
420 absorbance of the culture supernatant was measured at 420 nM using a SpectraMax M5 plate
421 reader (Molecular Devices).

422

423 **CnTps1 Protein expression and purification**

424 The full-length *TPS1* gene from *Cryptococcus neoformans* strain H99 was codon-
425 optimized for expression in *E. coli* (Genscript) and subcloned using ligation-independent cloning
426 into pMCSG7 (61). The construct was then transformed into *E. coli* OverExpress C41(DE3)
427 chemically competent cells engineered for high protein expression. Supernatants from lysed
428 cultures, induced with 0.5 mM IPTG, were loaded onto a nickel column (Ni-NTA, Qiagen) and
429 washed in a buffer (50 mM Tris pH 8.0, 300 mM NaCl, 5 mM $MgCl_2$ and 5% glycerol) and eluted
430 with increasing amounts of imidazole, which ranged from 40 mM to 400 mM imidazole, in this
431 buffer. The fractions containing 6xHis-CnTps1 were then pooled, concentrated to 5 mL, and run
432 over a S200 size exclusion column (HiLoad 26/600 Superdex 200pg, Cytiva) in pre-cooled buffer
433 containing 20 mM Tris pH 8.0, 300 mM NaCl, 5% glycerol and 2 mM β-mercaptoethanol. Size
434 exclusion fractions containing 6xHis-CnTps1 were pooled and concentrated to 1 mg/mL for
435 downstream experimental applications such as cryo-electron microscopy and activity assays.

436

437 **CnTps1 Cryo-EM grid preparation**

438 6xHis-CnTps1 was purified as described above and concentrated in a buffer containing
439 20 mM Tris pH 8.0, 300 mM NaCl, 5% glycerol and 2 mM β-mercaptoethanol. For grids prepared

440 with *apo* CnTps1, 3 µL of 0.75 mg/mL 6xHis-CnTps1 was applied to glow-discharged carbon
441 Quantifoil grids. After a 15 s incubation, the grids were blotted for 2 s to remove excess protein
442 and rapidly plunged into liquid ethane (-182 °C) using a Leica EM GP2 (Leica Microsystems)
443 operated at 95% humidity and 22 °C. For determination of the structure of the CnTps1-UDP-G6P
444 complex, 0.5 mg/mL 6xHis-CnTps1 was incubated with 10 mM uridine di-phosphate (UDP,
445 Sigma) and 10 mM glucose-6-phosphate (G6P, Sigma) for 18 hours at 4 °C. 3 µL of the CnTps1-
446 UDP-G6P mixture was deposited onto glow-discharged UltrAuFoil grids. After a 15 s incubation,
447 the grids were blotted for 2 s to remove excess protein and rapidly plunged into liquid ethane (-
448 182 °C) using a Leica EM GP2 (Leica Microsystems) operated at 95% humidity and 22 °C. Grids
449 were transferred to liquid nitrogen for storage until data collection.
450
451 **CnTps1 cryo-EM data collection**
452 After screening for high grid quality, using a Talos Arctica cryo-electron microscope
453 (Thermo Fisher Scientific), a total of 2,520 micrographs from the cryo-EM grids containing *apo*
454 CnTps1 were collected on a Titan Krios cryo-electron microscope (Thermo Fisher Scientific), at
455 300 kV equipped with a K3 detector (Gatan) at a nominal magnification of 105,000x and defocus
456 values from -2.5 µm to -0.8 µm. The pixel size was 0.65 Å. The total dose was 62 $e^{-}$ $Å^{-2}$.
457 The cryo-EM grids containing CnTps1-UDP-G6P were also screened on a Talos Arctica
458 cryo-electron microscope (Thermo Fisher Scientific). A total of 3,182 micrographs of CnTps1-
459 UDP-G6P were collected on a Titan Krios cryo-electron microscope (Thermo Fisher Scientific),
460 at 300 kV equipped with a K3 detector (Gatan) at a nominal magnification of 81,000x and defocus
461 values from -2.5 µm to -0.8 µm. The pixel size was 1.08 Å. The total dose was 62 $e^{-}$ $Å^{-2}$.
462
463 **Cryo-EM data processing**
464 For *apo* CnTps1, 2,520 dose-fractionated image stacks were aligned using the drift
465 correction routines implemented in RELION3.0 (62) and the contrast transfer function was
466 determined on the motion corrected non-dose-weighted sum of frames using CTFFIND4.1 (63).
467 CnTps1 particles were boxed out using template-free Auto-picking in RELION3.0. Two
468 consecutive rounds of 2D classification were preformed to obtain a clean set of particles. The
469 initial model was generated in RELION3.0, and 3 rounds of 3D classification were performed with
470 resulting reconstructions showing non-uniform angular distributions. To improve the alignment,
471 907 micrographs were selected with the CTF max fitting resolution cutoff as 4 Å. A total of 456,020
472 4x binned clean particles were used for further processing. A new *ab initio* 3D reference was
473 generated using 16,000 particles followed by 3D classification, and particles were classified into

474 5 classes. 207,081 particle images corresponding to best class were kept and subjected to 3D
475 refinement without symmetry resulting in a 5.3 Å resolution map. Particles were then re-centered
476 and re-extracted without binning and further refined using a shape mask to ~3.6 Å resolution.
477 After CTF refinement and Bayesian polishing in RELION3.0, the polished particles were imported
478 into cryoSPARC (64). Homogeneous refinement was performed without imposing symmetry
479 resulting in resolution of 3.6 Å. After imposing D2 symmetry, the final global resolution of the
480 reconstruction improved to 3.3 Å. A summary of the data processing steps is shown in
481 Supplemental Figure 3.
482 For determination of the structure of CnTps1 bound to UDP-G6P, dose-fractionated
483 movies were aligned with MotionCor2 (65) and CTF estimation was performed using
484 CTFFIND4.1. Aligned micrographs were sorted and selected according to max fitting resolution
485 with cutoff as 4 Å with cryoSPARC Curate Exposures yielding 2,617 images. CnTps1 particles
486 were boxed out with template-free Blob picker. Approximately, 2.8 million particles were extracted
487 and subjected to 2D classification using a circular mask (180 Å radius) to focus the alignment on
488 one monomer. A total of 2,079,376 clean particles were selected and subjected to *ab initio*
489 Reconstruction using 4 classes. A conformationally homogeneous class showed well resolved
490 features and accounted for ~850k particles which were kept and subjected to 3D refinement
491 (without imposing symmetry) resulting in a 3.1 Å resolution map. To improve the density of the
492 flexible loops around the substrate binding cave, 3D variability analysis was conducted using
493 cryoSPARC, and the particles were classified into 8 clusters. Further non-uniform refinement
494 using only particles assigned to cluster 1 resulted in the best map (3.5 Å resolution) that showed
495 well-resolved features on the flexible loop region. A summary of the data processing steps is
496 shown in Supplemental Figure 6.
497
498 **Cryo-EM model building**
499 Model building of the *apo* CnTps1 structure was initiated by using the CaTps2 N-terminal
500 domain crystal structure (PDB ID 5XDF) as the starting model. α-helix 2 had to be rebuilt. CnTps1
501 residues were mutated to match the correct sequence using COOT (66). Coordinates were then
502 fitted manually in Coot (66) followed by iterative refinement using Phenix (67) real space
503 refinement to improve the quality of the models. Following completion of the model of a single
504 protomer, multiple copies of the models were generated and docked into the map, using UCSF
505 Chimera 1.14, to form the homo-tetramer (68). The CnTps1-UDP-G6P model was generated
506 using the same workflow. The exception is that the initial model of the complex was the *apo*
507 CnTps1 model.

508 **Tps1 Activity Assay**

509 The catalytic activity of Tps1 was measured utilizing a continuous enzyme coupled assay
510 as previously reported (69). Briefly, 6xHis-CnTps1 protein was concentrated in a buffer containing
511 20 mM Tris pH 8.0, 300 mM NaCl, 5% glycerol and 2 mM β-mercaptoethanol. The assay was
512 carried out in a buffer containing 50 mM HEPES, pH 7.8, 100 mM KCl, 5 mM $MgCl_2$ and 2 mM
513 DTT. A final concentration of 3 μM, 1 mM and 1 mM were utilized for Tps1, uridine di-phosphate
514 glucose and glucose-6-phosphate, respectively. When reported, UDP-Galactose (UDP-Gal,
515 Sigma) was used in the assay. Activity assays were performed in clear, flat-bottomed 96-well
516 plates and the decrease in absorbance at 340 nm was recorded using a SpectraMax M5 plate
517 reader (Molecular Devices). The decrease in absorbance at 340 nm was analyzed for the 200 s
518 of the reaction, which corresponds to the initial rate of the reaction.

519

520 **Circular Dichroism spectroscopy**

521 Far-UV CD spectra of CnTps1 ΔIDD were recorded on an AVIV 435 CD
522 Spectrophotometer in a 1 mm sample cell. Measurements were taken from 200 to 260 nm with a
523 wavelength step of 1.0 nm and a 1 s averaging time. Each spectrum is the average of 3 scans.
524 CnTps1 ΔIDD was buffer exchanged into CD buffer (20 mM $NaH_2PO_4$ (pH 7.5), 300 mM NaF and
525 5% glycerol) and concentrated to a final concentration of 0.5 mg/mL.

526

527

528 **Accession Numbers**

529 Cryo-EM density maps of *apo* CnTps1 and CnTps1-UDP-G6P have been deposited in the
530 Electron Microscopy Databank (EMDB) with accession codes EMD-29338 and EMD-29172,
531 respectively. Atomic models of *apo* CnTps1 and CnTps1-UDP-G6P have been deposited in the
532 RCSB Protein Data Bank (PDB) with accession codes PDB ID 8FO1 and PDB ID 8FHW,
533 respectively.

534

535 **Acknowledgements**

536 This work was funded by grant 1P01AI104533 from the U.S. National Institutes of Health
537 to R.G.B. and the NIH Tri-Institutional Molecular Mycology and Pathogenesis Training Grant
538 T32AI052080 to E.W. Cryo-EM grid preparation and screening were carried out at the Genome
539 Integrity and Structural Biology Laboratory at the National Institute of Environmental and Health
540 Sciences in Research Triangle Park, NC. Cryo-EM data collection was performed at the Duke
541 University Shared Materials Instrumentation Facility (SMIF), a member of the North Carolina
542 Research Triangle Nanotechnology Network (RTNN), which is supported by the National Science
543 Foundation as part of the National Nanotechnology Coordinated Infrastructure (NNCI) (Grant
544 ECCS-2025064). We thank Dr. Mark Walters, Allen Hsu, and Megan Kopp for cryo-EM data
545 collection support. We thank Dr. Brady Travis for cryo-EM data processing support. This study
546 utilized the computational resources offered by Duke Research Computing.

547

548 **Author Contributions**

549 E.J.W. and R.G.B. designed the experiments and analyzed the biochemical data. E.J.W.,
550 Y.Z., A.B., and R.G.B. analyzed the structural data. E.J.W. generated purification constructs,
551 purified proteins, determined their structures and performed biochemical characterizations. M.P.,
552 A.H., Y.Z., M.J.B. and A.B. provided cryo-EM consulting and experimental input. E.J.W., Y.Z. and
553 R.G.B. wrote the manuscript with significant input from A.B. All authors have read and approved
554 the manuscript.

555

556 **Conflict of Interest Statement**

557 The authors declare that they have no conflict of interest.

558 **Figure Legends**

559

560 **Figure 1. Trehalose-6-phosphate synthase (Tps1) from *Cryptococcus neoformans* self-**
561 **associates. A)** Schematic of the canonical trehalose biosynthesis pathway in fungi. **B)** Bacterial
562 two-hybrid results indicate a self-association of LexA-CnTps1$_{56\text{-}669}$ by a reduction in β-galactoside
563 activity after induction of expression with 1 mM IPTG. Error bars represent standard error of
564 triplicate biological replicates (N=3). Statistically significant differences were demonstrated with
565 an unpaired Student's *t*-test (**** $P < 0.0001$). **C)** Anti-LexA Western blot confirms the expression
566 of LexA-CnTps1$_{56\text{-}669}$.

567

568 **Figure 2. Structure of the *apo Cryptococcus neoformans* Tps1 homo-tetramer.**
569 **A)** Structure of the *apo C. neoformans* Tps1 homo-tetramer. The density map is shown in grey,
570 overlayed with the model as a ribbon diagram. The protomers are colored and labelled in light
571 blue, green, navy and magenta. The dimensions of the "front" view of the tetramer are labelled in
572 Å. **B)** Structure of the tetramer viewed after a 90° rotation around the vertical axis. **C)** Structure of
573 the tetramer viewed after a 90° rotation around the horizontal axis. **D)** Ribbon diagram of a single
574 protomer of the *apo* CnTps1 cryo-EM structure with the N and C-termini labelled.

575

576 **Figure 3. Structure of the *Cryptococcus neoformans* Tps1 homo-tetramer bound to UDP**
577 **and G6P.**
578 **A)** Structure of the *C. neoformans* Tps1 homo-tetramer bound to UDP and G6P. The density map
579 is shown in grey, overlayed with the model as a ribbon diagram. The protomers are colored and
580 labelled in light blue, green, navy and magenta. The dimensions of the "front" view of the tetramer
581 are labelled in Å. Ligands UDP and G6P are shown with a space-filling representation. **B)**
582 Structure of the tetramer bound to UDP and G6P viewed after a 90° rotation around the vertical
583 axis. **C)** Structure of the tetramer bound to UDP and G6P viewed after a 90° rotation around the
584 horizontal axis. **D)** Ribbon diagram of a single protomer of the CnTps1-UDP-G6P structure with
585 the N and C-termini labelled and ligands in the substrate-binding pocket shown as atom-colored,
586 space-filling molecules.

587

588 **Figure 4. The binding of UDP and G6P induces a conformational change in CnTps1. A)**
589 Overlay of the *apo* CnTps1 protomer (light blue) with the CnTps1 protomer bound to UDP and
590 G6P (green). Density (grey mesh) is shown around ligands UDP and G6P in the substrate-binding
591 pocket. Position of α-helix 2 is indicated with a black box. **B)** Overlay of the *apo* CnTps1 protomer

592 (light blue) with CnTps1-UDP-G6P (green) viewed after a 90° rotation around the horizontal axis.
593 Electron microscopy density is shown with UDP and G6P in the substrate-binding pocket. The
594 position of α-helix 2 is boxed, with the black line demonstrating the movement of approximately 7
595 Å.
596
597 **Figure 5. Substrate-binding residues of CnTps1. A)** Cryo-EM density for UDP and G6P, shown
598 as light grey mesh. UDP and G6P are shown as atom-colored sticks. **B)** View of the CnTps1
599 residues involved in binding UDP. UDP and residues of the C-terminal domain are shown as
600 atom-colored sticks. Hydrogen bonds are shown by dashes. Key atoms of the UDP molecule are
601 labelled. **C)** View of CnTps1 residue R453, which binds G6P. G6P and CnTps1 R453 are shown
602 as atom-colored sticks. Hydrogen bonds are shown by dashes. **D)** Relative activity of wild-type
603 CnTps1 and UDP-binding mutants. Error bars represent the standard error of three independent
604 measurements. **E)** Relative activity of wild-type CnTps1 and the G6P-binding mutant R453A.
605 Error bars represent the standard error of three independent measurements.
606
607 **Figure 6. The CnTps1 substrate-binding pocket is highly specific for UDPG. A)** Relative
608 activity of wild-type CnTps1 utilizing either 1 mM UDPG or 1 mM UDP-Gal or UDP as substrates.
609 Error bars represent the standard error of three independent measurements. **B)** Relative activity
610 of wild-type CnTps1 with 1 mM UDPG and increasing concentrations of UDP-Gal. Error bars
611 represent the standard error of three independent measurements. 1 mM G6P is present in all
612 experiments.

613 **References**

614


615 1. G. D. Brown *et al.*, Hidden killers: human fungal infections. *Science translational medicine*
616 **4**, 165rv113 (2012).
617 2. F. Bongomin, S. Gago, R. O. Oladele, D. W. Denning, Global and Multi-National
618 Prevalence of Fungal Diseases-Estimate Precision. *J Fungi (Basel)* **3** (2017).
619 3. Anonymous, Stop neglecting fungi. *Nat Microbiol* **2**, 17120 (2017).
620 4. A. Alanio, S. Delliere, S. Fodil, S. Bretagne, B. Megarbane, Prevalence of putative invasive
621 pulmonary aspergillosis in critically ill patients with COVID-19. *Lancet Respir Med* **8**, e48-
622 e49 (2020).
623 5. J. P. Gangneux, M. E. Bougnoux, E. Dannaoui, M. Cornet, J. R. Zahar, Invasive fungal
624 diseases during COVID-19: We should be prepared. *J Mycol Med* **30**, 100971 (2020).
625 6. M. Hoenigl, Invasive Fungal Disease complicating COVID-19: when it rains it pours.
626 *Clinical infectious diseases : an official publication of the Infectious Diseases Society of*
627 *America* 10.1093/cid/ciaa1342 (2020).
628 7. P. Koehler *et al.*, COVID-19 associated pulmonary aspergillosis. *Mycoses* **63**, 528-534
629 (2020).
630 8. E. F. J. Meijer, A. S. M. Dofferhoff, O. Hoiting, J. B. Buil, J. F. Meis, Azole-Resistant
631 COVID-19-Associated Pulmonary Aspergillosis in an Immunocompetent Host: A Case
632 Report. *J Fungi (Basel)* **6** (2020).
633 9. D. Moser *et al.*, COVID-19 Impairs Immune Response to Candida albicans. *Front Immunol*
634 **12**, 640644 (2021).
635 10. B. Posteraro *et al.*, Pan-Echinocandin-Resistant Candida glabrata Bloodstream Infection
636 Complicating COVID-19: A Fatal Case Report. *J Fungi (Basel)* **6** (2020).
637 11. Y. Lee, E. Puumala, N. Robbins, L. E. Cowen, Antifungal Drug Resistance: Molecular
638 Mechanisms in Candida albicans and Beyond. *Chem Rev* **121**, 3390-3411 (2021).
639 12. J. R. Perfect, The antifungal pipeline: a reality check. *Nature reviews. Drug discovery* **16**,
640 603-616 (2017).
641 13. J. R. Perfect, G. M. Cox, Drug resistance in Cryptococcus neoformans. *Drug resistance*
642 *updates : reviews and commentaries in antimicrobial and anticancer chemotherapy* **2**,
643 259-269 (1999).
644 14. E. V. LeBlanc, E. J. Polvi, A. O. Veri, G. G. Prive, L. E. Cowen, Structure-guided
645 approaches to targeting stress responses in human fungal pathogens. *The Journal of*
646 *biological chemistry* **295**, 14458-14472 (2020).
647 15. J. R. Perfect, J. L. Tenor, Y. Miao, R. G. Brennan, Trehalose pathway as an antifungal
648 target. *Virulence* 10.1080/21505594.2016.1195529, 1-7 (2016).
649 16. K. M. Pianalto, J. A. Alspaugh, New Horizons in Antifungal Therapy. *J Fungi (Basel)* **2**
650 (2016).
651 17. A. Thammahong, S. Puttikamonkul, J. R. Perfect, R. G. Brennan, R. A. Cramer, Central
652 Role of the Trehalose Biosynthesis Pathway in the Pathogenesis of Human Fungal
653 Infections: Opportunities and Challenges for Therapeutic Development. *Microbiology and*
654 *molecular biology reviews : MMBR* **81** (2017).
655 18. N. Benaroudj, D. H. Lee, A. L. Goldberg, Trehalose accumulation during cellular stress
656 protects cells and cellular proteins from damage by oxygen radicals. *The Journal of*
657 *biological chemistry* **276**, 24261-24267 (2001).
658 19. J. H. Crowe, L. M. Crowe, J. F. Carpenter, C. Aurell Wistrom, Stabilization of dry
659 phospholipid bilayers and proteins by sugars. *The Biochemical journal* **242**, 1-10 (1987).
660 20. J. H. Crowe, L. M. Crowe, D. Chapman, Preservation of membranes in anhydrobiotic
661 organisms: the role of trehalose. *Science* **223**, 701-703 (1984).

662 21. J. H. Crowe, F. A. Hoekstra, L. M. Crowe, Anhydrobiosis. *Annu Rev Physiol* **54**, 579-599
663 (1992).
664 22. O. Fernandez, L. Bethencourt, A. Quero, R. S. Sangwan, C. Clement, Trehalose and plant
665 stress responses: friend or foe? *Trends Plant Sci* **15**, 409-417 (2010).
666 23. T. Hottiger, T. Boller, A. Wiemken, Rapid changes of heat and desiccation tolerance
667 correlated with changes of trehalose content in Saccharomyces cerevisiae cells subjected
668 to temperature shifts. *FEBS Lett* **220**, 113-115 (1987).
669 24. T. Hottiger, C. De Virgilio, M. N. Hall, T. Boller, A. Wiemken, The role of trehalose
670 synthesis for the acquisition of thermotolerance in yeast. II. Physiological concentrations
671 of trehalose increase the thermal stability of proteins in vitro. *Eur J Biochem* **219**, 187-193
672 (1994).
673 25. B. R. Steen *et al.*, Cryptococcus neoformans gene expression during experimental
674 cryptococcal meningitis. *Eukaryotic cell* **2**, 1336-1349 (2003).
675 26. A. D. Elbein, Y. T. Pan, I. Pastuszak, D. Carroll, New insights on trehalose: a
676 multifunctional molecule. *Glycobiology* **13**, 17R-27R (2003).
677 27. E. W. Petzold *et al.*, Characterization and regulation of the trehalose synthesis pathway
678 and its importance in the pathogenicity of Cryptococcus neoformans. *Infection and*
679 *immunity* **74**, 5877-5887 (2006).
680 28. P. Ngamskulrungroj *et al.*, The trehalose synthesis pathway is an integral part of the
681 virulence composite for Cryptococcus gattii. *Infection and immunity* **77**, 4584-4596 (2009).
682 29. M. Martinez-Esparza *et al.*, Role of trehalose-6P phosphatase (TPS2) in stress tolerance
683 and resistance to macrophage killing in Candida albicans. *Int J Med Microbiol* **299**, 453-
684 464 (2009).
685 30. P. Van Dijck, L. De Rop, K. Szlufcik, E. Van Ael, J. M. Thevelein, Disruption of the Candida
686 albicans TPS2 gene encoding trehalose-6-phosphate phosphatase decreases infectivity
687 without affecting hypha formation. *Infection and immunity* **70**, 1772-1782 (2002).
688 31. O. Zaragoza, M. A. Blazquez, C. Gancedo, Disruption of the Candida albicans TPS1 gene
689 encoding trehalose-6-phosphate synthase impairs formation of hyphae and decreases
690 infectivity. *Journal of bacteriology* **180**, 3809-3815 (1998).
691 32. N. Al-Bader *et al.*, Role of trehalose biosynthesis in Aspergillus fumigatus development,
692 stress response, and virulence. *Infection and immunity* **78**, 3007-3018 (2010).
693 33. S. Puttikamonkul *et al.*, Trehalose 6-phosphate phosphatase is required for cell wall
694 integrity and fungal virulence but not trehalose biosynthesis in the human fungal pathogen
695 Aspergillus fumigatus. *Molecular microbiology* **77**, 891-911 (2010).
696 34. M. D. Asencion Diez *et al.*, The Production and Utilization of GDP-glucose in the
697 Biosynthesis of Trehalose 6-Phosphate by Streptomyces venezuelae. *The Journal of*
698 *biological chemistry* **292**, 945-954 (2017).
699 35. J. C. Errey *et al.*, Mechanistic insight into enzymatic glycosyl transfer with retention of
700 configuration through analysis of glycomimetic inhibitors. *Angewandte Chemie* **49**, 1234-
701 1237 (2010).
702 36. J. D. Farelli *et al.*, Structure of the trehalose-6-phosphate phosphatase from Brugia malayi
703 reveals key design principles for anthelmintic drugs. *PLoS pathogens* **10**, e1004245
704 (2014).
705 37. R. P. Gibson, C. A. Tarling, S. Roberts, S. G. Withers, G. J. Davies, The donor subsite of
706 trehalose-6-phosphate synthase: binary complexes with UDP-glucose and UDP-2-deoxy-
707 2-fluoro-glucose at 2 A resolution. *The Journal of biological chemistry* **279**, 1950-1955
708 (2004).
709 38. R. P. Gibson, J. P. Turkenburg, S. J. Charnock, R. Lloyd, G. J. Davies, Insights into
710 trehalose synthesis provided by the structure of the retaining glucosyltransferase OtsA.
711 *Chemistry & biology* **9**, 1337-1346 (2002).

39. C. M. Harvey *et al.*, Structural Analysis of Binding Determinants of Salmonella typhimurium Trehalose-6-phosphate Phosphatase Using Ground-State Complexes. *Biochemistry* **59**, 3247-3257 (2020).
40. Y. Miao *et al.*, Structural and In Vivo Studies on Trehalose-6-Phosphate Synthase from Pathogenic Fungi Provide Insights into Its Catalytic Mechanism, Biological Necessity, and Potential for Novel Antifungal Drug Design. *mBio* **8** (2017).
41. Y. Miao *et al.*, Structures of trehalose-6-phosphate phosphatase from pathogenic fungi reveal the mechanisms of substrate recognition and catalysis. *Proceedings of the National Academy of Sciences of the United States of America* **113**, 7148-7153 (2016).
42. S. Shan, H. Min, T. Liu, D. Jiang, Z. Rao, Structural insight into dephosphorylation by trehalose 6-phosphate phosphatase (OtsB2) from Mycobacterium tuberculosis. *FASEB J* **30**, 3989-3996 (2016).
43. S. Wang *et al.*, Crystal structures of Magnaporthe oryzae trehalose-6-phosphate synthase (MoTps1) suggest a model for catalytic process of Tps1. *The Biochemical journal* **476**, 3227-3240 (2019).
44. M. Cross *et al.*, A suicide inhibitor of nematode trehalose-6-phosphate phosphatases. *Sci Rep* **9**, 16165 (2019).
45. S. Kapil, C. Petit, V. N. Drago, D. R. Ronning, S. J. Sucheck, Synthesis and in Vitro Characterization of Trehalose-Based Inhibitors of Mycobacterial Trehalose 6-Phosphate Phosphatases. *Chembiochem* **20**, 260-269 (2019).
46. C. Kern *et al.*, Trehalose-6-phosphate synthase from the cat flea Ctenocephalides felis and Drosophila melanogaster: gene identification, cloning, heterologous functional expression and identification of inhibitors by high throughput screening. *Insect molecular biology* **21**, 456-471 (2012).
47. S. Klutts *et al.*, Purification, cloning, expression, and properties of mycobacterial trehalose-phosphate phosphatase. *The Journal of biological chemistry* **278**, 2093-2100 (2003).
48. C. Liu, D. Dunaway-Mariano, P. S. Mariano, Rational design of reversible inhibitors for trehalose 6-phosphate phosphatases. *European journal of medicinal chemistry* **128**, 274-286 (2017).
49. Y. T. Pan, A. D. Elbein, Inhibition of the trehalose-P synthase of mycobacteria by various antibiotics. *Archives of biochemistry and biophysics* **335**, 258-266 (1996).
50. M. Dmitrova *et al.*, A new LexA-based genetic system for monitoring and analyzing protein heterodimerization in Escherichia coli. *Mol Gen Genet* **257**, 205-212 (1998).
51. L. L. Lairson, B. Henrissat, G. J. Davies, S. G. Withers, Glycosyltransferases: structures, functions, and mechanisms. *Annu Rev Biochem* **77**, 521-555 (2008).
52. L. Holm, P. Rosenstrom, Dali server: conservation mapping in 3D. *Nucleic Acids Res* **38**, W545-549 (2010).
53. R. A. Lee, M. Razaz, S. Hayward, The DynDom database of protein domain motions. *Bioinformatics* **19**, 1290-1291 (2003).
54. G. P. Poornam, A. Matsumoto, H. Ishida, S. Hayward, A method for the analysis of domain movements in large biomolecular complexes. *Proteins* **76**, 201-212 (2009).
55. S. S. Lee *et al.*, Mechanistic evidence for a front-side, SNi-type reaction in a retaining glycosyltransferase. *Nature chemical biology* **7**, 631-638 (2011).
56. E. Krissinel, K. Henrick, Inference of macromolecular assemblies from crystalline state. *Journal of molecular biology* **372**, 774-797 (2007).
57. W. Bell *et al.*, Composition and functional analysis of the Saccharomyces cerevisiae trehalose synthase complex. *The Journal of biological chemistry* **273**, 33311-33319 (1998).
58. A. Reinders *et al.*, Structural analysis of the subunits of the trehalose-6-phosphate synthase/phosphatase complex in Saccharomyces cerevisiae and their function during heat shock. *Molecular microbiology* **24**, 687-695 (1997).

763 59. A. Thammahong, A. K. Caffrey-Card, S. Dhingra, J. J. Obar, R. A. Cramer, Aspergillus
764 fumigatus Trehalose-Regulatory Subunit Homolog Moonlights To Mediate Cell Wall
765 Homeostasis through Modulation of Chitin Synthase Activity. *mBio* **8** (2017).
766 60. D. A. Daines, R. P. Silver, Evidence for multimerization of neu proteins involved in
767 polysialic acid synthesis in Escherichia coli K1 using improved LexA-based vectors.
768 *Journal of bacteriology* **182**, 5267-5270 (2000).
769 61. W. H. Eschenfeldt, S. Lucy, C. S. Millard, A. Joachimiak, I. D. Mark, A family of LIC vectors
770 for high-throughput cloning and purification of proteins. *Methods in molecular biology* **498**,
771 105-115 (2009).
772 62. S. H. Scheres, RELION: implementation of a Bayesian approach to cryo-EM structure
773 determination. *J Struct Biol* **180**, 519-530 (2012).
774 63. A. Rohou, N. Grigorieff, CTFFIND4: Fast and accurate defocus estimation from electron
775 micrographs. *J Struct Biol* **192**, 216-221 (2015).
776 64. A. Punjani, J. L. Rubinstein, D. J. Fleet, M. A. Brubaker, cryoSPARC: algorithms for rapid
777 unsupervised cryo-EM structure determination. *Nature methods* **14**, 290-296 (2017).
778 65. S. Q. Zheng *et al.*, MotionCor2: anisotropic correction of beam-induced motion for
779 improved cryo-electron microscopy. *Nature methods* **14**, 331-332 (2017).
780 66. P. Emsley, K. Cowtan, Coot: model-building tools for molecular graphics. *Acta*
781 *crystallographica. Section D, Biological crystallography* **60**, 2126-2132 (2004).
782 67. P. D. Adams *et al.*, PHENIX: a comprehensive Python-based system for macromolecular
783 structure solution. *Acta crystallographica. Section D, Biological crystallography* **66**, 213-
784 221 (2010).
785 68. E. F. Pettersen *et al.*, UCSF Chimera--a visualization system for exploratory research and
786 analysis. *J Comput Chem* **25**, 1605-1612 (2004).
787 69. J. C. Errey *et al.*, Mechanistic Insight into Enzymatic Glycosyl Transfer with Retention of
788 Configuration through Analysis of Glycomimetic Inhibitors. *Angew. Chem.-Int. Edit.* **49**,
789 1234-1237 (2010).
790 70. A. Idnurm, J. L. Reedy, J. C. Nussbaum, J. Heitman, Cryptococcus neoformans virulence
791 gene discovery through insertional mutagenesis. *Eukaryotic cell* **3**, 420-429 (2004).
792 71. J. A. Fraser, R. L. Subaran, C. B. Nichols, J. Heitman, Recapitulation of the sexual cycle
793 of the primary fungal pathogen Cryptococcus neoformans var. gattii: implications for an
794 outbreak on Vancouver Island, Canada. *Eukaryotic cell* **2**, 1036-1045 (2003).
795 72. D. L. Toffaletti, T. H. Rude, S. A. Johnston, D. T. Durack, J. R. Perfect, Gene transfer in
796 Cryptococcus neoformans by use of biolistic delivery of DNA. *Journal of bacteriology* **175**,
797 1405-1411 (1993).
798

799 **Figure 1**

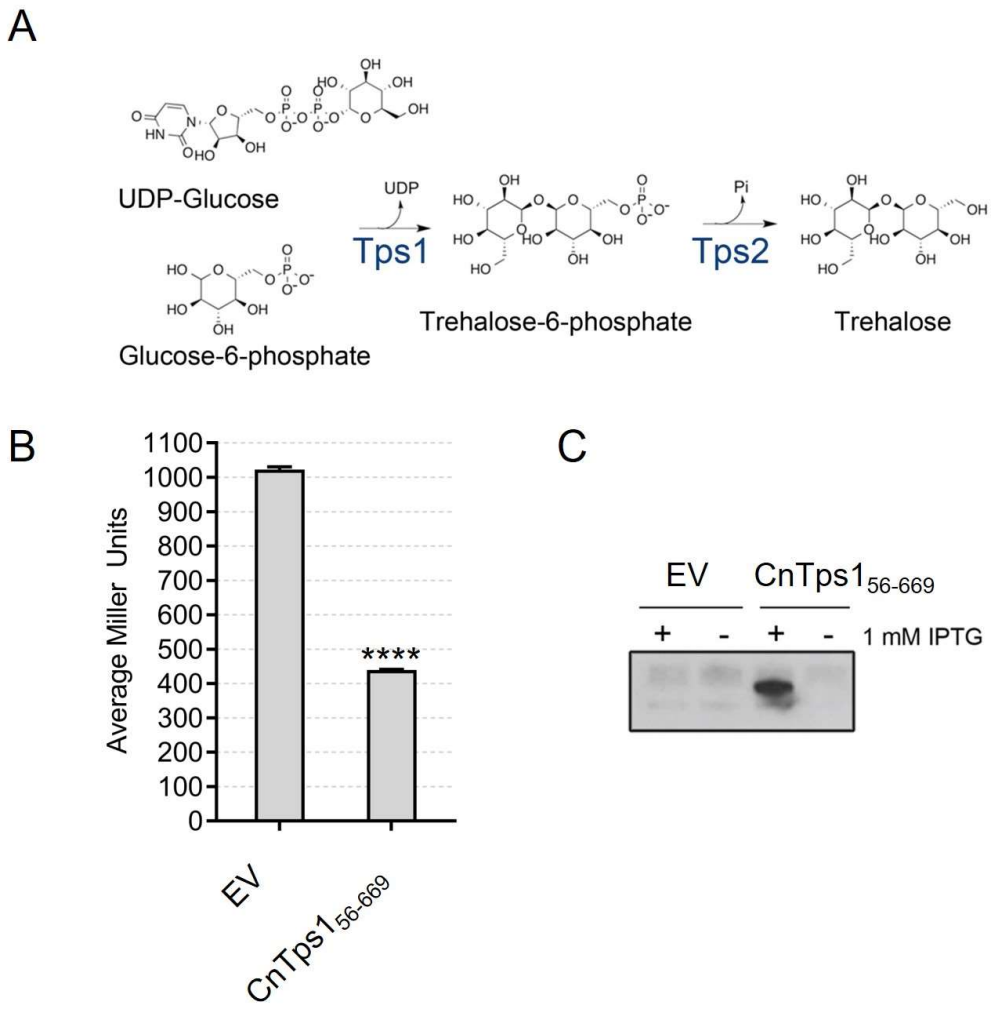
A
UDP-Glucose
Glucose-6-phosphate
UDP
Tps1
Trehalose-6-phosphate
Pi
Tps2
Trehalose
B
Average Miller Units
1100
1000
900
800
700
600
500
400
300
200
100
0
****
EV
CnTps1 56-669
C
EV
CnTps1 56-669
+
-
+
-
1 mM IPTG

**Figure 2**

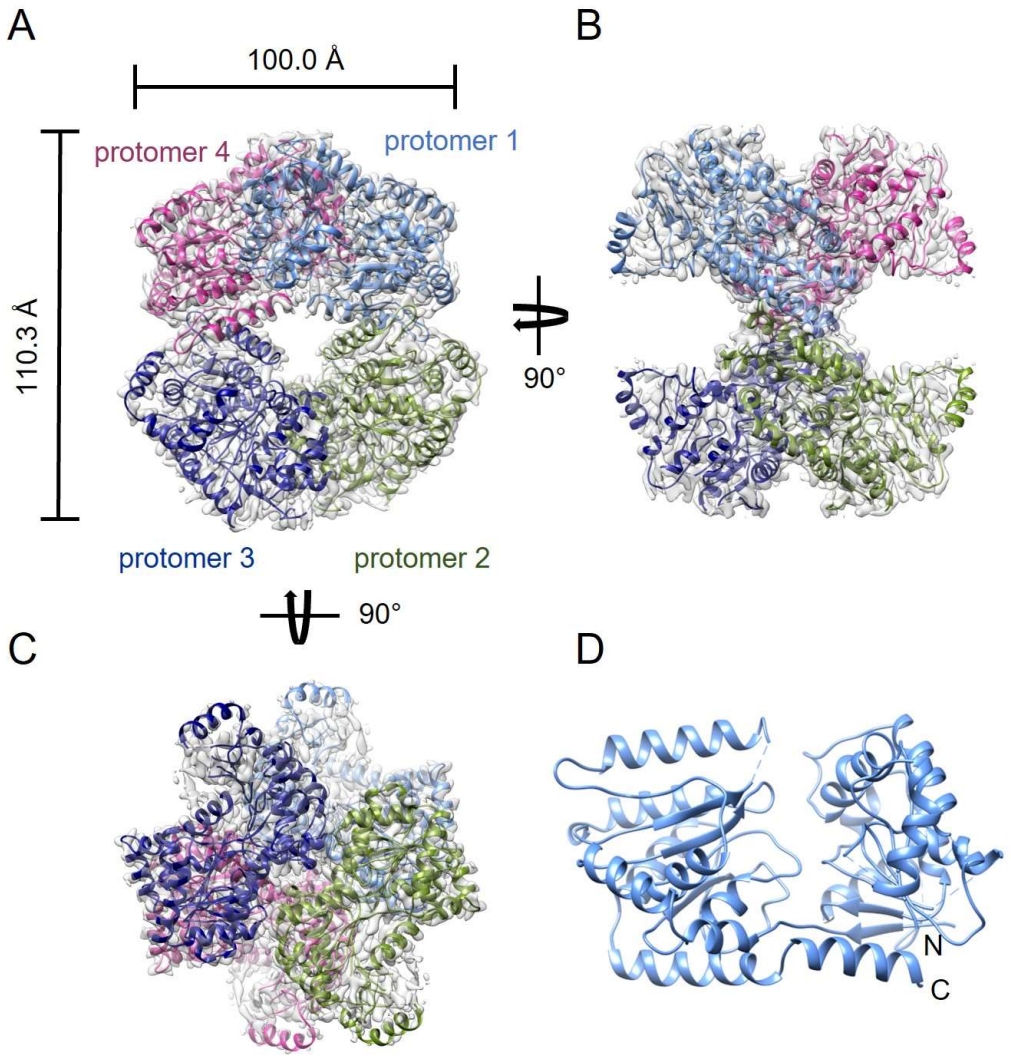
A
100.0 Å
110.3 Å
protomer 4
protomer 1
protomer 3
protomer 2
B
90°
C
90°
D
N
C

**Figure 3**

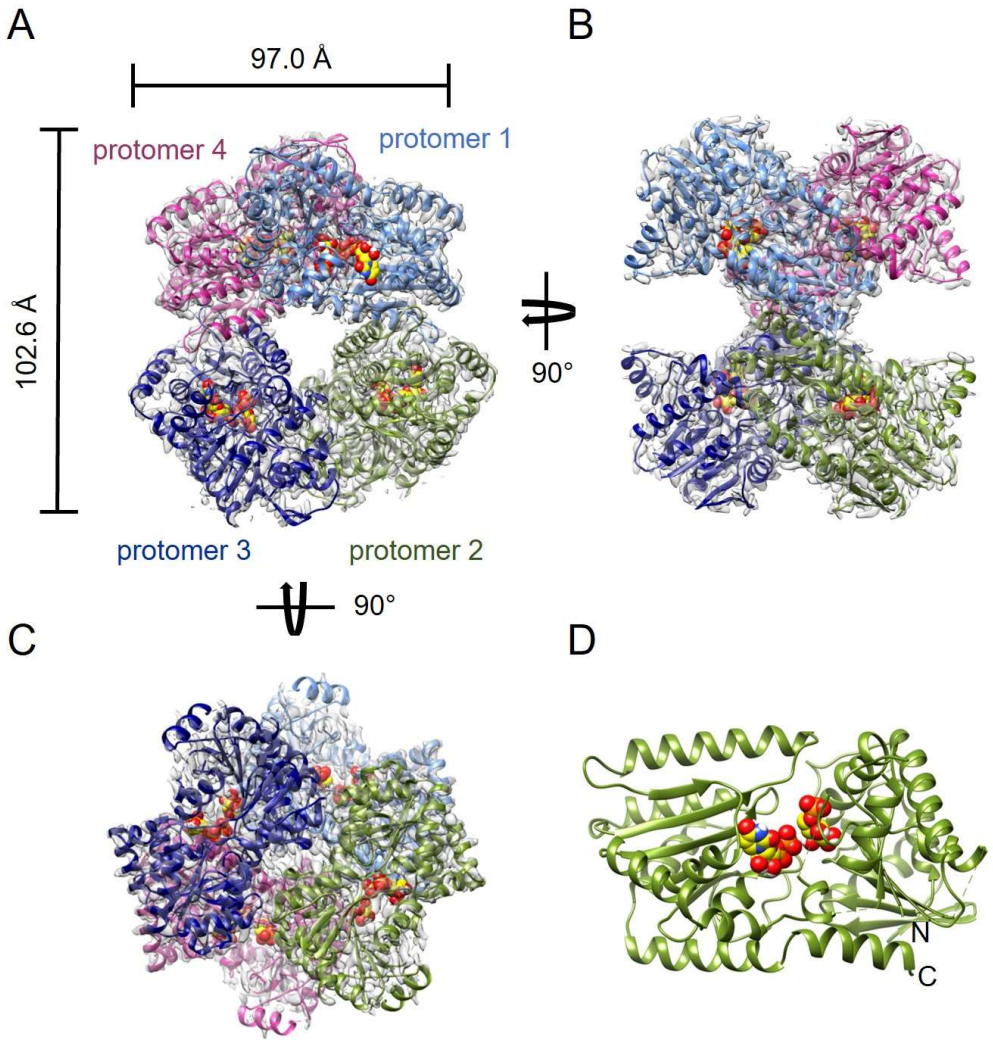
A
97.0 Å
102.6 Å
protomer 4
protomer 1
protomer 3
protomer 2
90°
B
90°
C
D
N
C

**Figure 4**

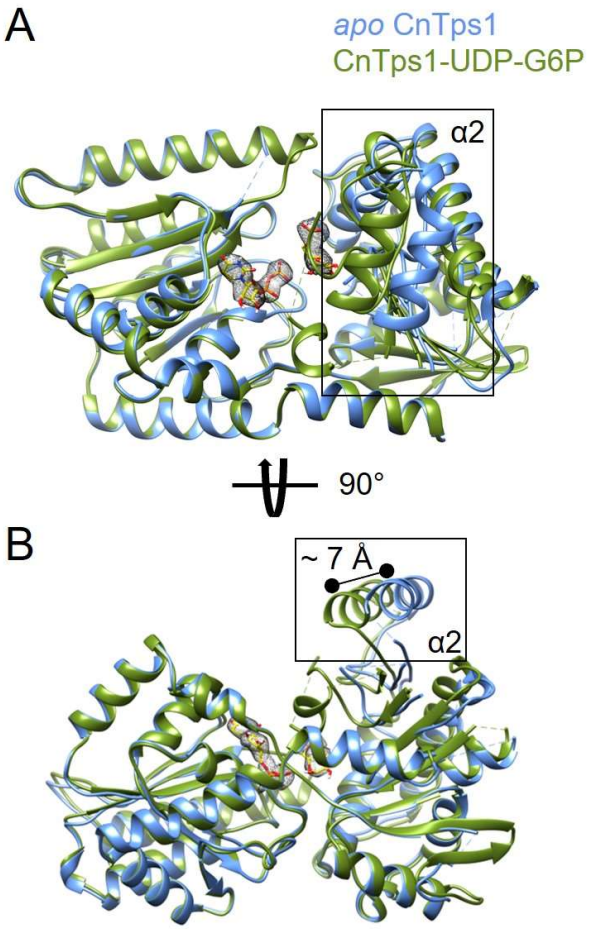

**Figure 5**

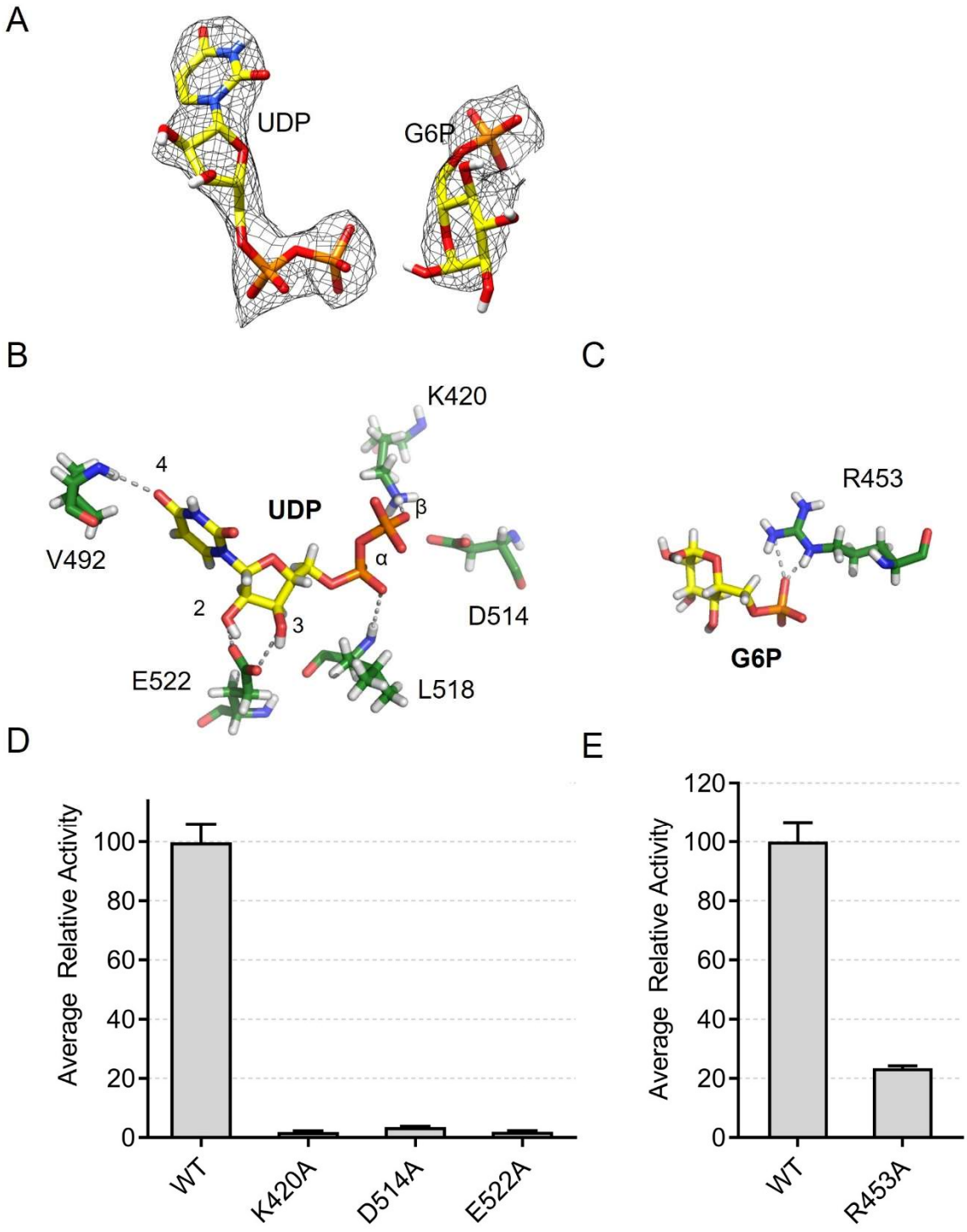
A
UDP
G6P
B
K420
4
UDP
β
V492
α
2
3
D514
E522
L518
C
R453
G6P
D
Average Relative Activity
100
80
60
40
20
0
WT
K420A
D514A
E522A
E
Average Relative Activity
120
100
80
60
40
20
0
WT
R453A

**Figure 6**

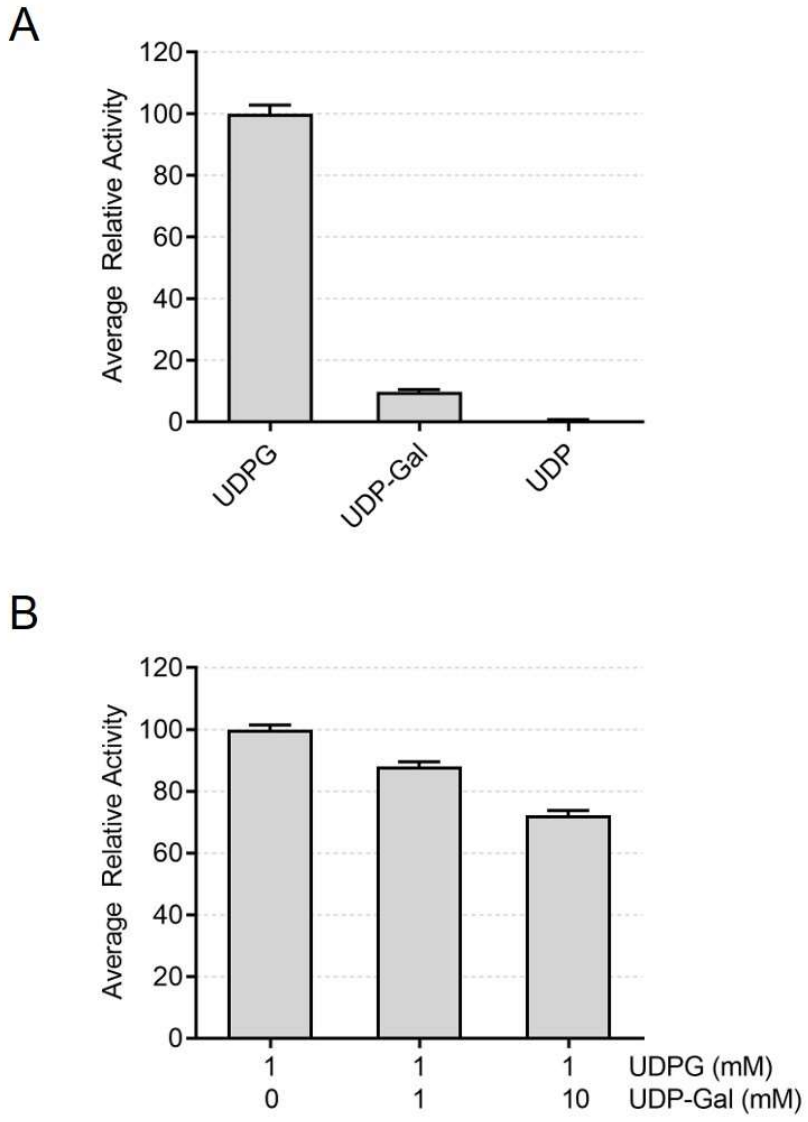
A
Average Relative Activity
120
100
80
60
40
20
0
UDPG
UDP-Gal
UDP
B
Average Relative Activity
120
100
80
60
40
20
0
1 1 1 UDPG (mM)
0 1 10 UDP-Gal (mM)